

Influence of inert gases on the reactive high power pulsed magnetron sputtering process of carbon-nitride thin films

Susann Schmidt, Zsolt Czigány, Grzegorz Greczynski, Jens Jensen, and Lars Hultman

Citation: *J. Vac. Sci. Technol. A* **31**, 011503 (2013); doi: 10.1116/1.4769725

View online: <http://dx.doi.org/10.1116/1.4769725>

View Table of Contents: <http://avspublications.org/resource/1/JVTAD6/v31/i1>

Published by the AVS: Science & Technology of Materials, Interfaces, and Processing

Related Articles

The Si₃N₄/TiN Interface: 4. Si₃N₄/TiN(001) Grown with a -250 V Substrate Bias and Analyzed In situ using Angle-resolved X-ray Photoelectron Spectroscopy
[Surf. Sci. Spectra 19, 62 \(2012\)](#)

The Si₃N₄/TiN Interface: 1. TiN(001) Grown and Analyzed In situ using Angle-resolved X-ray Photoelectron Spectroscopy
[Surf. Sci. Spectra 19, 33 \(2012\)](#)

The Si₃N₄/TiN Interface: 5. TiN/Si₃N₄ Grown and Analyzed In situ using Angle-resolved X-ray Photoelectron Spectroscopy
[Surf. Sci. Spectra 19, 72 \(2012\)](#)

The Si₃N₄/TiN Interface: 6. Si/TiN(001) Grown and Analyzed In situ using Angle-resolved X-ray Photoelectron Spectroscopy
[Surf. Sci. Spectra 19, 82 \(2012\)](#)

The Si₃N₄/TiN Interface: 2. Si₃N₄/TiN(001) Grown with a -7 V Substrate Bias and Analyzed In situ using Angle-resolved X-ray Photoelectron Spectroscopy
[Surf. Sci. Spectra 19, 42 \(2012\)](#)

Additional information on J. Vac. Sci. Technol. A

Journal Homepage: <http://avspublications.org/jvsta>

Journal Information: http://avspublications.org/jvsta/about/about_the_journal


Top downloads: http://avspublications.org/jvsta/top_20_most_downloaded

Information for Authors: http://avspublications.org/jvsta/authors/information_for_contributors

ADVERTISEMENT

Instruments for advanced science

Gas Analysis




- dynamic measurement of reaction gas streams
- catalysis and thermal analysis
- molecular beam studies
- dissolved species probes
- fermentation, environmental and ecological studies

Surface Science



- UHV TPD
- SIMS
- end point detection in ion beam etch
- elemental imaging - surface mapping

Plasma Diagnostics



- plasma source characterization
- etch and deposition process reaction kinetic studies
- analysis of neutral and radical species

Vacuum Analysis



- partial pressure measurement and control of process gases
- reactive sputter process control
- vacuum diagnostics
- vacuum coating process monitoring

contact Hiden Analytical for further details

HIDEN ANALYTICAL

info@hideninc.com
www.HidenAnalytical.com

CLICK to view our product catalogue 

Influence of inert gases on the reactive high power pulsed magnetron sputtering process of carbon-nitride thin films

Susann Schmidt^{a)}

Thin Film Physics Div., Department of Physics (IFM), Linköping University, SE-581 83, Sweden

Zsolt Czigány^{b)}

Institute of Technical Physics and Materials Science, Research Centre for Natural Sciences, Hungarian Academy of Sciences, Konkoly Thege Miklós út 29-33. H-1121 Budapest, Hungary

Grzegorz Greczynski,^{c)} Jens Jensen,^{d)} and Lars Hultman^{e)}

Thin Film Physics Div., Department of Physics (IFM), Linköping University, SE-581 83, Sweden

(Received 13 September 2012; accepted 15 November 2012; published 7 December 2012)

The influence of inert gases (Ne, Ar, Kr) on the sputter process of carbon and carbon-nitride (CN_x) thin films was studied using reactive high power pulsed magnetron sputtering (HiPIMS). Thin solid films were synthesized in an industrial deposition chamber from a graphite target. The peak target current during HiPIMS processing was found to decrease with increasing inert gas mass. Time averaged and time resolved ion mass spectroscopy showed that the addition of nitrogen, as reactive gas, resulted in less energetic ion species for processes employing Ne, whereas the opposite was noticed when Ar or Kr were employed as inert gas. Processes in nonreactive ambient showed generally lower total ion fluxes for the three different inert gases. As soon as N₂ was introduced into the process, the deposition rates for Ne and Ar-containing processes increased significantly. The reactive Kr-process, in contrast, showed slightly lower deposition rates than the nonreactive. The resulting thin films were characterized regarding their bonding and microstructure by x-ray photoelectron spectroscopy and transmission electron microscopy. Reactively deposited CN_x thin films in Ar and Kr ambient exhibited an ordering toward a fullerene-like structure, whereas carbon and CN_x films deposited in Ne atmosphere were found to be amorphous. This is attributed to an elevated amount of highly energetic particles observed during ion mass spectrometry and indicated by high peak target currents in Ne-containing processes. These results are discussed with respect to the current understanding of the structural evolution of a-C and CN_x thin films. © 2013 American Vacuum Society. [http://dx.doi.org/10.1116/1.4769725]

I. INTRODUCTION

The possibility to tailor the microstructure and thus properties of carbon-based thin films for a variety of applications justifies intense research.^{1–5} Especially, diamond-like carbon (DLC) and fullerene-like carbon nitride (FL-CN_x) roused interest due to their different outstanding mechanical properties. DLC possesses superior wear resistance, hardness, chemical inertness,^{2,6–8} and biocompatibility,⁹ whereas FL-CN_x exhibits an enormous resiliency (elastic recovery of up to 98%), low wear and friction.^{10,11} This combination of properties presents FL-CN_x as an ideal material for wear resistant applications. Since the properties of both materials are determined by the energy of film forming species during synthesis, we start by a short review of the current understanding. For DLC, the mechanical properties depend on the variation of the *sp*³/*sp*²-C bonding ratio. An increased amount of *sp*³-bonds leads to high hardness, approaching that of diamond.^{3,12,13} Lifshitz *et al.*¹⁴ described the formation of *sp*³ bonds by a local densification and subsequent relaxation of the C network during high energy ion bombardment

[30–100 eV (Refs. 12, 15, and 16)]. Such deposition conditions are supplied by magnetron sputtering, arc deposition, or ion-beam deposition. In this context, the advantages of high power impulse magnetron sputtering (HiPIMS also known as HPPMS) should be considered as this deposition method generates an increased amount and energy of the ionized target material, due to a high temporal electron density in the HiPIMS plasma.^{17,18} Despite the comparatively high ionization potential (*I*_P = 11.26 eV, Table I) and low sputter yield (0.197 atoms/ion for 500 eV Ar ions in the C/Ar discharge) of C, an enhanced amount and energy of C⁺ was as well found for the C discharge in HiPIMS-mode.¹⁹ Nevertheless, the ionized flux fraction of C in HiPIMS remains rather low at 4.5%.²⁰ Sarakinos *et al.* showed an increase in the amount of *sp*³-bonds of up to 50% for DLC films prepared by HiPIMS²¹ compared to DCMS (direct current magnetron sputtering). Petrov *et al.*²² reported higher C ion energies and, in correlation to this, also increased electron temperatures during magnetron sputtering of C in Ne compared to Ar, whereas the inert gas ion-to-C neutral arrival rates were found to be similar for both inert gases. Aijaz *et al.* suggested the utilization of Ne as inert gas while sputtering a graphite target in HiPIMS mode, leading to an increased electron temperature.²³ The authors claimed a subsequent increase in C⁺ energy and flux, causing higher amounts of *sp*³-bonds in C films. The impact of sputter mode and inert gas on the

^{a)}Electronic mail: sussc@ifm.liu.se

^{b)}Electronic mail: czigany.zsolt@ttk.mta.hu

^{c)}Electronic mail: grzgr@ifm.liu.se

^{d)}Electronic mail: jejen@ifm.liu.se

^{e)}Electronic mail: larhu@ifm.liu.se

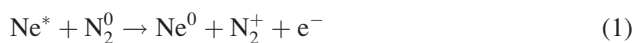
TABLE I. Collection of process relevant data for C/inert gas/N₂-discharges.

	Inert gases			Reactive gas species		Target material
	Ne	Ar	Kr	N ₂	N	C
1st ionization energy (eV), I_p	21.56	15.75	13.99	15.6	14.53	11.26
Total ionization cross section (10^{-17} cm ²) at 25 eV	0.25 (Ref. 58)	16.5 (Ref. 58)	19.5 (Ref. 58)		1.17 (Ref. 59)	14.4 (Ref. 59)
Metastable excitation energy (eV) (Ref. 43)	16.62 16.71	11.55 11.72	9.91 9.99			
Total sputter yield for C (atoms/ion) at 100 eV ^a	0.02	0.005	0.0001	0.009	0.04	0.07

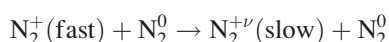
^aAs obtained by TRIM (Ref. 60) simulations for ion energies of 100 eV and incidence angles of 0° with respect to the target surface.

chemical bonding of the C and C-based films can thus be considered substantial.

Sputtering with different inert gases while keeping the same reactive gas and target material implies changes to plasma and process parameters generally because of differences in collision cross sections, momentum transfer, and ionization/excitation energies. Particularly, differences in sputter yield, electron-impact ionization cross sections, inert gas ionization energies (I_p), as well as metastable excitation energies are of interest (Table I). Apart from the sputter yield, these parameters influence electron impact ionization and Penning ionization (ionization due to metastable inert gas atoms)—the two major ionization mechanisms in the PVD plasma. Moreover, the plasma electron temperature is influenced by I_p of the process gasses; increasing I_p implicates an increased mean electron energy contributing to ionization.^{22,24} Therefore, the amount and the energy of ions in the plasma are affected as well. Different inert gases also determine the way secondary electrons are created²⁵ with respect to relative contributions from inert gas ions, recoils, and electrons. In the case when graphite is sputtered in Ne, electrons and ions contribute to the electron yield to approximately equal parts of ~40% and ~60%, respectively. If Kr is used as inert gas, contributions to the electron yield of ions dominate (~80%), recoiled atoms play an increased role (~10%) and, in this case, a lower contribution for electrons (~10%) was calculated.²⁵ Adding N₂, as reactive gas, to the Ne discharge one of the major metal ionization mechanisms in PVD—the Penning ionization—was found to play a considerable role for the ionization of N₂.²⁶ In Ne/N₂ discharges with N₂ contents up to 50% a Penning mixture²⁷ is formed. The ability of Ne to Penning ionize N₂ according to^{26,28}



is attributed to the metastable states of Ne (Ne*) at 16.62 and 16.67 eV that exceed the ionization potential of N₂ ($I_p = 15.6$ eV) and N ($I_p = 14.53$ eV). In the cathode sheath, the conversion of kinetic energy to vibration/excitation and dissociation of molecular nitrogen may occur in the two steps:



and



where ν represents vibration excitation energy. The dissociative charge transfer (2) has threshold energy of ~24 eV.²⁸ Also possible are ionization and dissociation of N₂ due to electron impact or the ionization due to charge transfer from inert gas ions.²⁸ However, the existence of several metastable states of N₂ allows manifold ionization and dissociation pathways.²⁹ Generally, for low-pressure discharges the process gas ionization (Ne, Ar, Kr, N₂) is likely to be governed by electron impact ionization.

The evolution of the distinct FL-CN_x microstructure was first described theoretically by Gueorguiev *et al.*³⁰ and arises due to the incorporation of N into the C-matrix, causing the formation of pentagon defects and this in turn provokes a bending and cross linking of the graphene sheets. Those bent cross linked graphene sheets give rise to the outstanding mechanical properties of this material. From an experimental point of view, the mechanism behind the structural evolution of FL-CN_x—chemical sputtering—was first reported by Hellgren *et al.*⁴ and later theoretically explained by Schluter *et al.*³¹ Chemical sputtering is a temperature regulated chemical desorption process taking place at the growth surface procuring structure-defining C_xN_y⁺-species ($x, y \leq 2$). Recently, we published a comparative study, in which different HiPIMS and DCMS processes for the deposition of FL-CN_x thin films were evaluated. The study revealed that a mechanism that can be described as pulse assisted chemical sputtering during reactive HiPIMS of a graphite target promotes the structural evolution of CN_x thin films toward a FL structure and is taking place already at the target. Additionally, operating the graphite target with short, but high power pulses, as it is done in HiPIMS, produces an increased average energy and amount of C⁺, but also increased amounts of C_xN_y⁺-species.¹⁹

It becomes evident that HiPIMS process and plasma parameters are distinctly different for each of the gases and that a wide process window can be spanned in their utilization. Former DCMS studies on CN_x thin films presented the substrate temperature (T_s), the energy of film-forming ions, and the nitrogen-to-argon flow ratio $f_{\text{N}_2/\text{Ar}}$ as most important growth parameters in order to modify the CN_x thin film microstructure and thus properties.¹¹ We expect vast possibilities to control and influence CN_x thin film formation during HiPIMS. The role of different inert gases on reactive HiPIMS deposition of CN_x films is, however, unexplored. In

the presented study, we investigate the effect of three different inert gases (Ne, Ar, Kr) on HiPIMS process and plasma parameters as well as on the chemical bonding and microstructure of CN_x thin films. Conclusions on the growth as well as structure-defining mechanisms are drawn from the evaluation of the plasma processes (ion mass-spectrometry, target current waveforms) in combination with thin film characterization [high resolution transmission electron microscopy (HRTEM), selected area electron diffraction (SAED), and x-ray photo electron spectroscopy (XPS)].

II. EXPERIMENT DETAILS

Ion mass-spectrometry measurements and film depositions were carried out in an industrial CC800/9 coating system (CemeCon AG, Germany). Plasma characterization and film depositions were made in HiPIMS mode. Our investigations were performed using one rectangular target with an area of 440 cm^2 . Pure graphite targets (Tokai CARBON Deutschland GmbH) were sputtered in Ne, Ar, or Kr and additionally in inert gas/ N_2 atmosphere at a constant pressure of 400 mPa. The amount of N_2 in the working gas, defined by

$$\frac{f_{N_2}}{f_{\text{inert gas}} + f_{N_2}} \cdot 100\%, \quad (3)$$

where f_{N_2} and $f_{\text{inert gas}}$ represent the flow of N_2 and inert gas, respectively, ranged between 14% and 100%. In power-regulated mode a frequency of 300 Hz was applied. For ion mass spectrometry measurements of Ne-containing processes, an average power of 1800 W was applied to the cathode, whereas for processes involving Kr an average power of 1400 W was used. Reference measurements for both power settings (1400 and 1800 W) were conducted in an Ar-containing atmosphere. An average power of 1800 W was chosen for Ne-containing discharges due to the fact that more stable discharge conditions during ion mass spectroscopy measurements were achieved with this slightly higher average power. The pulse width was kept constant in all processes at $200 \mu\text{s}$. The measurements took place at room temperature. Furthermore, since the mass spectrometer orifice is grounded no additional bias voltage was applied.

IEDFs were measured in a time-averaged and time-resolved mode for the most abundant ionic plasma species, namely C^+ , C_2^+ , N^+ , N_2^+ , Ne^{++} , Ne^+ , Ar^+ , Ar^{++} , Kr^{++} , $^{82}Kr^+$, $^{84}Kr^+$, $^{86}Kr^+$, CN^+ , and $C_2N_2^+$. The measurements were performed with a PSM003 unit from Hidden Analytical, UK, operated with a quadrupole mass analyzer sensitive to masses up to 300 amu with a resolution of 0.1 amu. In order to allow comparisons, the measurements were carried out with identical global settings (including detector, extractor, and quadrupole voltages and currents) after fine-tuning with regards to mass 12, assigned to C^+ . The position of the spectrometer orifice relative to the target with regards to the angle as well as spatial and lateral was comparable to the arrangement of the substrates to the target. A distance of 60 mm between target and the spectrometer orifice was kept

similar for all measurements and corresponds also to the spacing between target and substrate during thin film deposition. Time-averaged data were recorded between -0.5 eV and 50 eV with step widths of 0.5 eV . The dwell time was set to 100 ms, which corresponds to an information depth of at least 30 pulses in each data point. Acquisitions for time-resolved ion mass-spectrometry measurements were triggered by the signal from a Tektronix DPO4054 500 MHz bandwidth digital oscilloscope. The delay time, related to the onset of the power pulse to the cathode, ranged from $40 \mu\text{s}$ up to $280 \mu\text{s}$ with an increment of $20 \mu\text{s}$. A total acquisition time of 1 ms per data point was applied. Time-resolved mass spectrometry was carried out for ion energies ranging between 0 and 30 eV with a resolution of 0.5 eV . The ion time-of-flight (TOF) within the mass spectrometer was corrected for presented time-resolved data, with the purpose to show the plasma composition at the spectrometer orifice (substrate surface) rather than at the spectrometers' detector. Therefore, the approach suggested by Bohlmark *et al.*³² was used. The plasma species and their calculated corresponding TOF are listed in Table II. Naturally, the TOF of ions within the mass spectrometer depends on their initial kinetic energy. However, for kinetic energies below 100 eV , the TOF varies not more than 10%. Since this is the case for the applied processes, a mean particle energy of 8 eV was used for all TOF calculations. During ion mass spectrometry measurements the target current and target voltage waveforms were recorded with a Tektronix DPO4054 500 MHz bandwidth digital oscilloscope.

Thin films were deposited on Si(001) substrates using an average power of 1400 W for all inert gases and inert gas/ N_2 mixtures. The above presented settings regarding the pulse width and frequency were used as well during deposition. In addition, a pulsed bias voltage (V_b) of -100 V , synchronized with the cathode high voltage pulse, was applied to the substrate table. Two different substrate temperatures (T_s) of 110°C and at 430°C were chosen for the thin film deposition. Thin films deposited at a low substrate temperature of 110°C were evaluated regarding their deposition rate (R_d) and N content, in order to allow comparisons with the results gained by plasma characterization. The effect of the inert gases on the structural evolution of the CN_x films is presented here for samples deposited at 430°C , since substrate

TABLE II. Measured ion species together with their mass/charge ratio and TOF correction.

Ion	m/e	TOF correction (μs)
C^+	12	32
C_2^+	24	45
CN^+	26	47
$C_2N_2^+$	52	67
Ne^+	20	41
Ne^{++}	10	29
Ar^+	40	59
Ar^{++}	20	41
$^{84}Kr^+$	84	85
Kr^{++}	42	60

temperatures above 300 °C were found to be necessary to form the FL-structure.^{33,34}

Deposition rates were determined with cross-sectional scanning electron microscopy (SEM, LEO 1550 Gemini, Zeiss, Germany). The composition of CN_x films were evaluated using time-of-flight elastic recoil detection analysis (ToF-ERDA) applying an 36 MeV ¹²⁷I⁹⁺ ion beam at 22.5° incidence angle relative to the surface.^{35,36} Here, data were stored event by event in list mode and analyzed off-line. Only the data obtained during the first minutes (yielding sufficient statistics) were used.

X-ray photoelectron spectroscopy (XPS) was performed with a Quantum 2000 spectrometer from PHI Physical Electronics, Inc., USA, using a monochromatic Al(K_α) X-ray beam ($h\nu = 1486.6$ eV) and a chamber pressure of less than 1.4×10^{-6} Pa. XPS data of the C1s, N1s, and O1s regions were collected after the samples were sputter-cleaned for 10 min with 500 eV Ar⁺ ions. The lowest sputter energy possible was chosen as the CN_x bonding structure was reported to be easily affected and might also be accompanied by a preferential sputtering of N.³⁷ Automatic charge compensation was applied, due to the fact that CN_x films typically show elevated electrical resistivities³⁸ compared to conducting materials. Obtained spectra were fitted using Voigt peak shape, with the Lorentzian contribution not exceeding 20%. The full width at half maximum (FWHM) was restricted to 1.7 eV for the main contributions C1 and C2 of the N1s core level spectra, whereas the FWHM of the minor contributions C3 and C4 was restricted to 2.0 eV. A Shirley-type background was used and all spectra were referenced to the C—C (C—CH) bond at 284.5 eV.

Cross-sectional TEM was carried out on cleaved samples.³⁹ These samples were examined in a Tecnai G2 TF 20 UT TEM (FEI, The Netherlands). SAED patterns were exposed with a CCD camera in the same instrument and processed with diffraction software.⁴⁰ The degree of structuring (fullerene-like, graphitic or amorphous) was assessed in evaluating peak intensities of the rings at ~ 3.5 Å and ~ 2 Å ($I_{3.5\text{Å}}$ and $I_{2\text{Å}}$), extracted from the SAED pattern. The relative peak intensity ($R = I_{3.5\text{Å}}/I_{2\text{Å}}$) describes the degree of graphitic short range ordering in CN_x and C-based materials.⁴¹

III. RESULTS AND DISCUSSION

A. Target current and target voltage waveforms for different inert gases

In order to investigate the effect of different inert gases on the sputter process for the deposition of a-C and CN_x thin films, the target current $I(t)$ and target voltage $U(t)$ waveforms are evaluated first. In the case of industrial HiPIMS processing operated on large-area cathodes, the shape of the target current and target voltage traces depends to large extent on the size of the capacitor bank of the pulsing unit. The resulting voltage pulse is far from an ideal, rectangular form, and often exhibits a sudden drop in amplitude with pulse time. Examples of such behavior can be seen in Fig. 1, where current and voltage waveforms for processes in pure

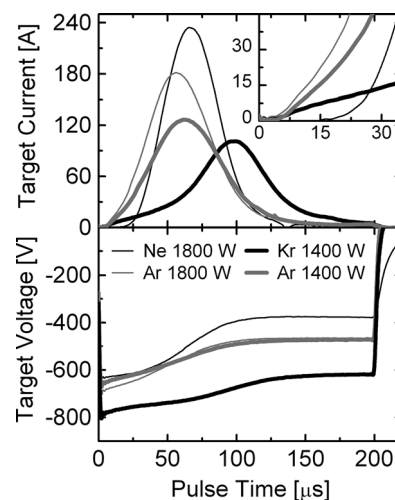


Fig. 1. Target current and target voltage waveforms for HiPIMS processes comparing different inert gases; Ne ($P_{\text{av}} = 1800$ W, black thin line) and the corresponding Ar process ($P_{\text{av}} = 1800$ W, gray thin line) as well as Kr ($P_{\text{av}} = 1400$ W, black bold line) with corresponding Ar process ($P_{\text{av}} = 1400$ W, gray bold line). The inset presents a magnification of the first 35 μs of $I(t)$ and depicts the delay in the raise of the target current.

Ne [cf. black thin line, $P_{\text{Tav}} = 1800$ W]) and pure Kr [cf. black bold line, $P_{\text{Tav}} = 1400$ W]) are presented. As reference, the corresponding $I(t)$ and $U(t)$ characteristics of equivalent processes (the same frequency, pressure, process temperature, and pulse duration) employing Ar for both power settings are additionally included in Fig. 1. Evident is the high peak target current (\hat{I}) of ~ 245 A as the graphite target is sputtered in pure Ne atmosphere in comparison to $\hat{I} \sim 180$ A for the process in pure Ar atmosphere. In contrast to this is the \hat{I} for the discharge in Kr, as it rises to ~ 100 A at an average power of 1400 W and is thus compared to $\hat{I} \sim 126$ A of the Ar discharge at 1400 W (cf. gray bold line Fig. 1) rather low.

The discharge current comprises ion and electron current. Increased \hat{I} values indicate in a first approximation elevated amounts of charged species that form in the vicinity of the target as different noble gases are used for the sputter process. Factors that influence the over-all amount of charged sputtered species and consequently contributing to \hat{I} are as follows:

- The sputter yield, as more particles are sputtered, the probability for ionization is enhanced. The sputter yield of carbon increases for the used noble gases in the sequence Kr, Ar, Ne (Table I).
- The first ionization potential I_P of the inert gas; an increased I_P implies elevated electron temperatures,^{22,24} contributing to ionization and thus, \hat{I} . The ionization potential increases with decreasing inert gas atomic number (Table I).
- The total ionization cross section for electron energies below 50 eV increase in the sequence Ne, Ar, and Kr, (Table I).⁴² Here, it should be taken into account that electron energies are possibly considerably higher for Ne processes²³ and decrease with increasing atomic number of the inert gas. Thus, differences in ionization cross sections may not be as crucial.

- (iv) The excitation energies of the metastable energy levels for the three inert gases increase with decreasing inert gas atomic number [Table I (Ref. 43)], whereas the excitation energies for Ar (11.55 and 11.72 eV) are just above the first ionization potential of C (11.26 eV). Therefore, it is reasonable to conclude that Penning excitation and ionization occurs only as the graphite target is sputtered in Ar and Ne atmosphere.
- (v) The secondary electron emission yield (γ_{SE})³³ is considered as well, as it merely depends on I_p of the used inert gas in the case the graphite target is sputtered in metallic mode. In order to estimate γ_{SE} , the empirical equation⁴⁴

$$\gamma_{SE} = 0.032(0.78 I_p - 2\varphi) \quad (4)$$

is valid for HiPIMS processes where particle energies are below 100 eV. In Eq. (4), I_p resembles the ionization potential of the impinging particles (sputter gas) on the target surface and φ the work function of the target material. A three times higher γ_{SE} was calculated for the C/Ne discharge compared to the C/Ar discharge. In case the graphite target is sputtered in Kr, γ_{SE} yielded 30% of the value for the C/Ar discharge. This is mirrored in the peak target current of the C discharge for the three different inert gases (Fig. 1).

Another remarkable feature is the delay in the onset of the target current pulse (cf. inset in Fig. 1). It is attributed to a number of process parameters such as gas pressure⁴⁵ and target material,⁴⁶ and the process gas composition.⁴⁷ In the presented study, the time dependence of the electrical breakdown (time lag until the target current rises) was observed for different inert gases as well as for different reactive process gas mixtures and is demonstrated in Figs. 1 (inset) and 2(a) and 2(b). Discharges in pure Ar and Kr show a delay of 6 μs , whereas the electrical breakdown for Ne was observed after 22 μs (inset, Fig. 1). Due to the comparatively high I_p and high metastable excitation energies of Ne, the energy loss of fast electrons is more substantial during the exciting and ionization of noble gas atoms, than for Kr and Ar.

Discharges in pure N_2 atmosphere yield an electrical breakdown delay of 9 μs and 15 μs for processes with an average power of 1800 and 1400 W, respectively. Hala *et al.*⁴⁰ investigated the $I(t)$ characteristics of Cr in a reactive Ar/ N_2 atmosphere thoroughly. They conclude that the delayed rise of the current is an indication of a delayed gas breakdown due to energy loss of electrons by excitation and dissociation of N_2 (electron quenching), since molecular nitrogen has several vibrational and rotational excitation levels that are accessible for energy absorption. However, for reactive carbon discharges involving N_2 , apart from electron quenching, rather complex sputter mechanisms occur at the target surface and in the vicinity of the target (i.e., chemical desorption processes, excitation and dissociation of nitrogen, and C_xN_y molecules). Additionally, not only the properties of the sputter gas are considered to be changed, but also those of the graphite target surface. Therefore, the onset delay of the current pulse in the case of N_2 and inert gas/ N_2 mixtures may have more than one explanation.

In Figs. 2(a) and 2(b), the current wave forms for reactive processes employing N_2 in different N_2 /inert gas [for N_2 /Ne,

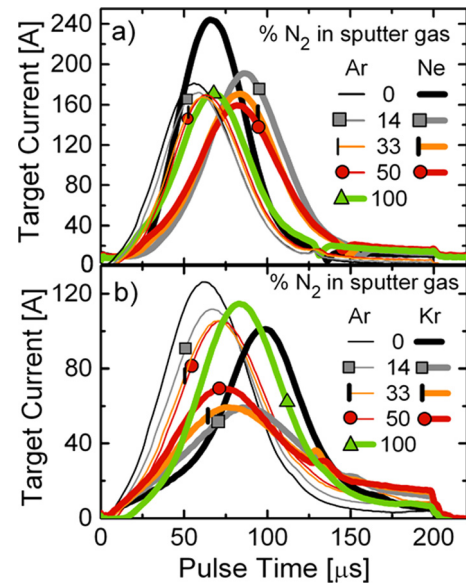


Fig. 2. (Color online) (a), (b) Target current waveforms for reactive HiPIMS processes comparing different N_2 contents in the inert gases; (a) $I(t)$ for discharges carried out at $P_{av} = 1800$ W in Ne/ N_2 (bold lines) and in Ar/ N_2 (thin lines); (b) $I(t)$ for discharges carried out at $P_{av} = 1400$ W in Kr/ N_2 (bold lines) and in Ar/ N_2 (thin lines).

N_2 /Ar, cf. Fig. 2(a) and N_2 /Ar, N_2 /Kr cf. Fig. 2(b)] mixtures are presented. For reactive processes in Ar or Ne [thin and bold lines, respectively, Fig. 2(a)], \hat{I} has a minimum as the process is carried out in $\sim 50\%$ N_2 with values of 166 and 160 A for Ar and Ne, respectively. The addition of more N_2 to the process gas mixture results in a slight increase of \hat{I} to 170 A as the graphite target is sputtered in pure N_2 . This accounts for 70% of the \hat{I} when pure Ne is used and is mainly attributed to differences in γ_{SE} as the sputter gas chemistry (different I_p of the inert gas/reactive gas mix), but additionally also the work function of the target changes. With the introduction of N_2 in the HiPIMS sputter process, the target surface chemistry changes, since dangling C bonds become passivated by nitrogen and a C-N surface layer builds up eventually. The acting mechanisms were investigated and explained in detail for the C/Ar/ N_2 system in Ref. 17 and are assumed to apply for the C/Kr/ N_2 and C/Ne/ N_2 sputter processes as well. Apart from differences in γ_{SE} , electron-quenching effects may contribute to the decreased \hat{I} values when N_2 is introduced into the reactive HiPIMS process, which were observed for the Ar, Ne, and Kr discharges. This quenching effect reduces the probability of electron impact ionization, since electrons lose their energy by excitation of N_2 .^{47,48}

The temporal evolution of \hat{I} is distinct; as it shifts toward the pulse end with the introduction of N_2 into the Ne discharge. A further increase of N_2 in the plasma ($>14\%$) causes the peak target current to appear early until it eventually emerges at the same pulse time (66 μs) similar to when the process is carried out in pure N_2 compared to the process in pure Ne. As graphite is sputtered in Kr [cf. Fig. 2(b)] mixtures, the opposite is recorded; the target current shows its maximum (~ 100 A) in the middle of the pulse (at ~ 101 μs). Here, an increase of the nitrogen content in the sputter gas

causes the target current to peak gradually earlier during the pulse. The temporal evolution observed in the $I(t)$ waveforms shown in Figs. 2(a) and 2(b) does not only depend on the time delay required for the current to rise (electrical breakdown). If corrected for this time delay, the instant the target current peaks still depends on the applied sputter gas as well as average power. In this context, the ionization and excitation mechanisms of N_2 , Kr, Ar, Ne, and C are important. Also, the rather complex sputter mechanisms, including next to physical sputtering also temperature dependent chemical desorption processes of C_xN_y species from the changed target surface¹⁹ should be considered.

B. Effects of inert gases on the ion composition of the C/ N_2 /inert gas HiPIMS discharge

Two main components are usually observed in time-averaged IEDFs recorded for HiPIMS processes; a low-energy portion that mirrors thermalized ions and a high-energy tail. This high-energy tail comprises three main components: the probability function of electron impact ionization, the probability function for collisions between target ions and inert gas neutrals, and the energy transmission function of the mass spectrometer.⁴⁹ Essentially, these components are observed in the present experiments; however, their fractions vary to a large extent in C plasmas of different inert gases.

Figures 3(a)–3(m) shows IEDFs of the most abundant species arriving at the substrate/orifice, recorded for discharges of graphite in different N_2 /Ne mixtures [Figs. 3(a)–3(f)] and

corresponding processes employing Ar [Figs. 3(g)–3(m)] instead of Ne. Most prominent are the IEDFs of C^+ and Ne^+ [Figs. 3(a) and 3(b)] obtained for 0% N_2 (black lines) 14% N_2 (gray lines) in the sputter gas. In both cases, a broad energy distribution of target and gas ions is evident. This is in contrast to the IEDFs obtained in reactive sputter mode employing $\geq 33\%$ N_2 . A further increase of the reactive gas content causes the high-energy tails in the IEDFs of C^+ , Ne^+ , and N^+ [Figs. 3(a), 3(b), and 3(f)] to move constantly toward lower energies, which is in contrast to the respective Ar processes [Figs. 3(g), 3(h), and 3(m)]. Here, IEDFs of C^+ , Ar^+ , and N^+ broaden slightly with the addition of reactive gas although not to the same extent. In fact, IEDFs of discharges involving Ne are more affected by the addition of N_2 than those for discharges involving Ar. This can be attributed to differences in nature of Ar and Ne with respect to N_2 and the effects of I_p on the discharge as discussed above.

Striking is the comparison of N_2^+ and N^+ IEDF's for the Ne discharge with 14% of N_2 [gray lines, Figs. 2(c) and 2(f)]; only a small quantity of N_2^+ ions at low energies (~ 2.5 eV) was recorded, whereas a comparatively large amount of N^+ ions with the high-energy tail peaking at ~ 23 eV was measured for the same process. This indicates enhanced ionization and dissociation mechanisms according to reactions (1) and (2) for N_2 in the Ne/ N_2 mixtures containing $\sim 14\%$ N_2 . Itagaki *et al.* correlated the electron temperature and density with the dissociation rate of N_2 in an ECR (electron cyclotron resonance) plasma and found for both parameters increased rates.⁵⁰ This in combination with increased plasma

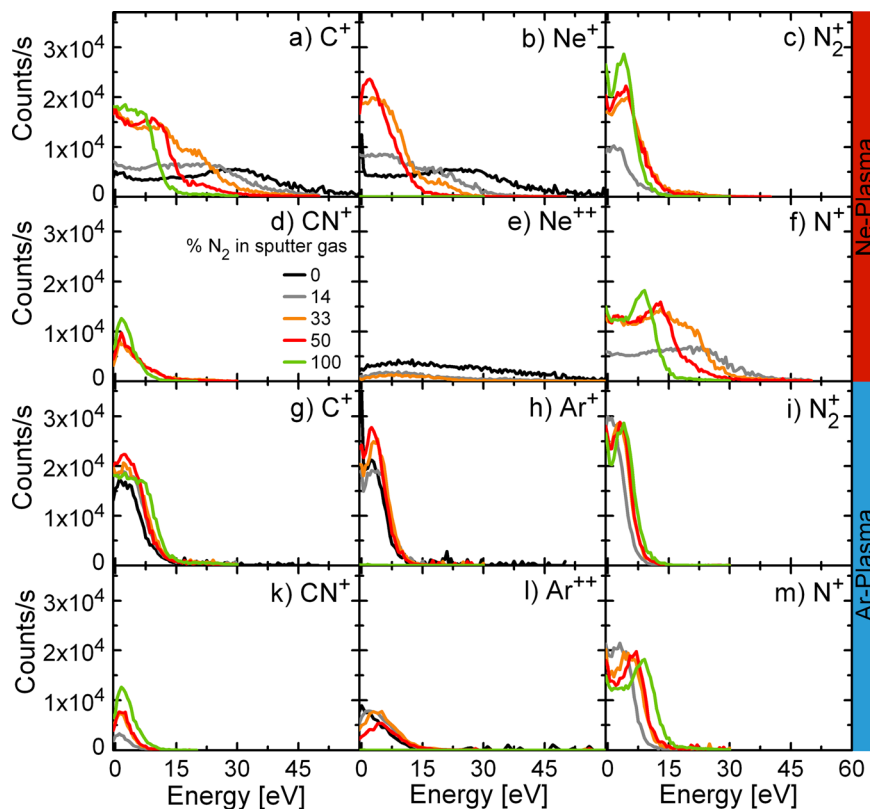


Fig. 3. (Color online) (a)–(m) Time-averaged IEDFs of the most abundant precursor species recorded for HiPIMS discharges at $P_{av} = 1800$ W in Ne and Ne/ N_2 [(a)–(f)] as well as Ar and Ar/ N_2 [(g)–(m)] of graphite.

temperatures due to the comparatively high I_P of Ne supports the assumption of Penning ionized N_2 due to Ne, undergoing a subsequent dissociative charge transfer [cf. reactions (1) and (2)].

Apart from this, IEDFs for CN^+ and N_2^+ of the Ne and the Ar plasma do not vary much in energy, merely the amount of ions increases with the increase of N_2 . Doubly charged Ne ions [Fig. 3(e)] show a broad distribution and low intensity but were only observed for processes up to 33% of N_2 in the sputter gas, whereas Ar^{++} ions [Fig. 3(l)] were recorded at lower energies peaking at a maximum of 5 eV for all presented Ar-containing processes. Due to the short distance of 60 mm between the target and the mass spectrometers orifice, the lowered collision probability in the Ne discharge and a relatively high average power of 1800 W, significant amounts of thermalized species were only observed for Ar^+ ions.

Figures 4(a)–4(f) present the comparison of IEDFs obtained from the most abundant precursor species of C discharges in Kr/ N_2 and Ar/ N_2 ambient for comparable process settings. Generally, IEDFs recorded for discharges carried out in Kr-containing atmosphere exhibit narrower energy distributions than the equivalent Ar processes. The C^+ signals [Fig. 4(a)] reside at comparable energies (~ 1.5 eV) as the N_2 content in the sputter gas increases and approaches 50% N_2 in the sputter gas. The process in pure N_2 atmosphere yields a broadening of the C^+ energy distribution peaking at ~ 3 eV. The respective Ar processes [Fig. 4(g)] yield C^+ energy distributions that are hardly affected by

increasing N_2 contents. Here, the IEDF values peak between 1.5 and 3.5 eV.

Examples for IEDFs of Kr-isotopes $^{84}Kr^+$ and $^{83}Kr^+$ are presented in Fig. 4(b) and 4(e), respectively, since the qualitative comparison of their shape can be used to verify the measurements. The distributions of both species show similar features, as should be the case, since both species origin from the same source (inert gas), and hardly vary in mass or dimension. The IEDFs of $^{84}Kr^+$ and $^{83}Kr^+$ are very narrow and consist of mainly thermalized ions with little dependence on the N_2 content in the sputter gas. Moreover, the relative abundance of the Kr-isotopes $^{82}Kr^+$, $^{83}Kr^+$, $^{84}Kr^+$, and $^{86}Kr^+$ (not shown here) was extracted from the corresponding distributions to yield in 13.8, 16.9, 54.2, and 15.0%, respectively. This is in fair agreement with data published by Yoon and Glab,⁵¹ for the respective abundances 11.6, 11.5, 57, and 17.3%. $^{78}Kr^+$ and $^{80}Kr^+$ were omitted in our measurements and their evaluation, due to their low abundance of 0.35% and 2.25%, respectively.⁵¹ In contrast to Kr^+ , broader distributions are obtained for Ar^+ under comparable process conditions in Ar-containing discharges. Here, the peak value of the high-energy tail moves from 5 to 2 eV as soon as N_2 is added to the process and remains there with the further increase of reactive gas [Fig. 4(h)]. It is noted that the difference in average power (1400 and 1800 W) for Ar-containing processes has no significant affect on ion energies of the recorded species. In all Kr-containing processes, doubly charged Kr ions (not shown here) were present and yielded $\sim 50\%$ of the energy compared to Ar^{++} [Fig. 4(l)].

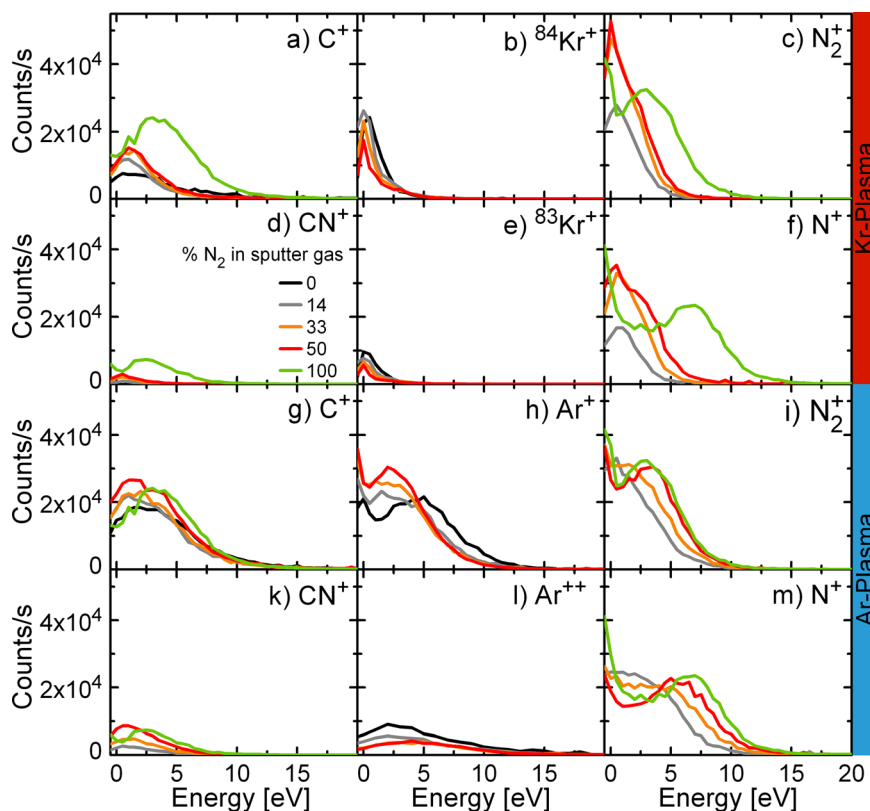


Fig. 4. (Color online) (a)–(m) Time-averaged IEDFs of the most abundant precursor species recorded for HiPIMS discharges at $P_{av} = 1400$ W in Kr and Kr/ N_2 [(a)–(f)] as well as Ar and Ar/ N_2 [(g)–(m)] of graphite.

Distributions of N_2^+ and N^+ , recorded for Kr and Ar-containing processes at 1400 W [Figs. 4(c), 4(f), 4(i), and 4(m), respectively], exhibit higher energies as the N_2 content in the sputter gas increases. This was also observed in IEDFs of N_2^+ and N^+ for the discharge of C/Ar/ N_2 at 1800 W. Similar processes in Ne-containing atmosphere showed the opposite effect; the mean energy of N^+ decreased as more N_2 is introduced. This demonstrates the effect of the Penning mixture as C is sputtered in Ne with small amounts of N_2 . Moreover, for Kr/ N_2 -containing processes with more than 14% N_2 significant portions of thermalized N_2^+ and N^+ were recorded, owing to the higher collision cross sections in the Kr/ N_2 plasma.

Figures 5(a) and 5(b) present the comparison on the ion flux of the most abundant precursor species of sputter processes using Ne and Ar, respectively, as a function of the nitrogen content. Here, data from time-averaged mass spectrometry were integrated over the entire energy range. For the C process in pure Ne, the ion fluxes of C^+ and Ne^+ ions are equal, showing a relative flux of $\sim 35\%$. C^{++} and Ne^{++} species were recorded with a relative abundance of 17% and 12%, respectively. This high amount of doubly charged species is a consequence of the high energetic C/Ne discharge, providing for the necessary energy to create such species. The comparison to the correspondent C/Ar process shows reduced ion fluxes for C^+ and Ar^+ . However, with respect to the C/Ne process the relative C^+ and Ar^+ ion fluxes are higher ($\sim 41\%$ and $\sim 48\%$, respectively), owing to the absence of C^{++} and the low relative flux of Ar^{++} ($\sim 10\%$).

With the introduction of N_2 to the processes, the total ion fluxes rise instantly for both inert gases with peak values at 33% of N_2 in the sputter gas (Fig. 5). The total ion flux is significantly higher when Ne is employed. For the Ne/ N_2 plasma between 14% N_2 and 50% N_2 in the sputter gas, mainly C^+ , N^+ and to a lower extent Ne^+ as well as N_2^+ is observed. The comparably high flux of C^+ is a consequence of the increased sputter yield for C in Ne in combination with elevated amounts and energies of electrons as well as

high metastable energy levels of Ne, providing an increased probability of ionization events due to electron impact and Penning ionization. This stands in contrast to the Ar/ N_2 plasma, where C^+ , N^+ , N_2^+ , and Ar^+ exist to equal amounts.

The doubly charged ion fluxes decrease continuously until they are hardly quantifiable when the process gas exceeds 33% N_2 in either Ne or Ar. In return the fluxes of C_xN_y species ($x, y \leq 2$) grow in magnitude. The CN^+ flux rises constantly with the N_2 content for Ar-containing discharges, but in Ne discharges it is first quantified at 33% of N_2 . C_xN_y species are a result of chemical sputtering (thermal desorption) at the target and substrate. For Ne/ N_2 -containing discharges ($N_2 < 33\%$), their formation may be hindered or C_xN_y species are dissociated by particles with high energies.

As the amount of inert gas decreases due to the increase of the N_2 fraction in the sputter gas the ion flux of the inert gases do not follow the expected trend; the flux of Ne^+ peaks at 33% and shows at 50% of N_2 a comparable value to the process as no reactive gas is used. A similar course is observed for the Ar^+ flux with peak values at 33% and 50% of N_2 in the sputter gas. This can be attributed to the overall increased amount of ions in the reactive process causing an additional ionization of the working gas. The comparatively high flux of N^+ ions is remarkable for the process in Ne/ N_2 atmosphere at 14% N_2 . With further addition of N_2 to the Ne process, the N^+/N_2^+ ion flux rate decreases continuously (2.7 at 14% N_2 , 1.6 at 33% N_2 , 1.4 at 50% N_2 , and 0.98 at 100% N_2 in the sputter gas), attributed to a lowered dissociation and ionization of N_2 as a consequence of decreasing amounts of Ne. Electron impact ionization and dissociation are likely to play a considerable role, too, because of the high γ_{SE} and electron temperature (high I_P) in discharges where Ne is the major part of the process gas. The above presented results suggest that the effects of both described ionization and dissociation pathways are significant as long as Ne is the major process gas (N_2 -contents $< 50\%$), which is supported by results from Avelar-Batista *et al.* investigating Ne- N_2 interactions in DC discharges by optical emission spectroscopy.²⁶ Moreover, in the case Ar is used, the relative flux of N^+ and N_2^+ is equal and does not change significantly over the entire range of reactive sputter processes (14% N_2 to 100% N_2).

The comparison on the ion flux of the most abundant plasma precursors for Kr and Ar containing processes is presented in Figs. 6(a) and 6(b), respectively. Here, a lower average power (1400 W) was applied, than for the comparison of Ne versus Ar (1800 W), since most stable process conditions were achieved by these settings for the different inert gases in the described process setup. The lower average power is mirrored in the Ar/ N_2 plasma by slightly reduced C^+ and CN^+ ion fluxes, whereas Ar^+ , N_2^+ , and N^+ [Fig. 6(b)] are comparable to corresponding fluxes extracted for the Ar/ N_2 plasma at 1800 W [Fig. 5(b)]. Therefore, the total, relative, and the sum of the ion fluxes for Ar processes employing 1400 W or 1800 W do not differ significantly. As can be drawn from Fig. 6(a), the total C^+ and Kr^+ fluxes are strikingly low in the Kr/ N_2 plasma. As the N_2 content rises,

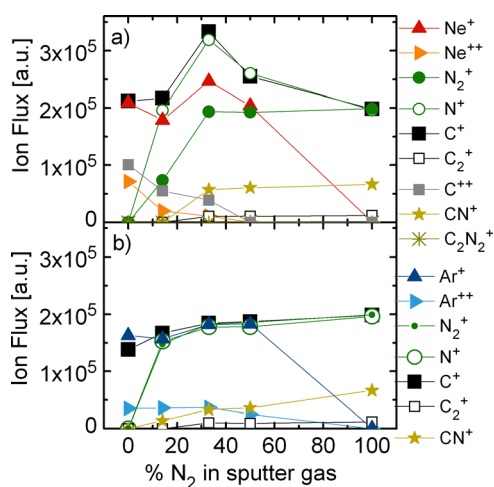


Fig. 5. (Color online) (a), (b) Ion fluxes in dependence of the nitrogen content in the inert gas for (a) Ne and (b) Ar-containing processes extracted from time averaged IEDFs of the corresponding processes.

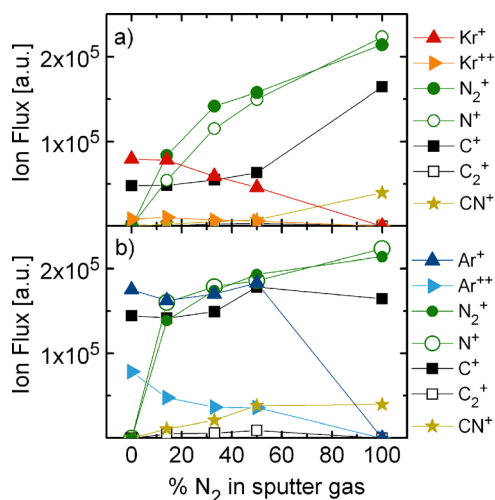


FIG. 6. (Color online) (a), (b) Ion fluxes in dependence of the nitrogen content in the inert gas for (a) Kr and (b) Ar-containing processes extracted from time averaged IEDFs of the corresponding processes.

the Kr^+ signal falls steadily, which is not observed for Ar- and Ne-containing processes up to 50% N_2 in the plasma. Possible causes may be the higher electron impact ionization cross section for N_2 implicating a lack of electrons with sufficient energy to ionize Kr. This would arise due to the low I_p of Kr, leading to a reduced γ_{SE} and electrons of decreased energy. In addition, the electron quenching due to the presence of N_2 should be considered in this respect. Moreover, it implies that ions and electrons generated by the ionization of the rising N_2 content cannot contribute significantly to the ionization of Kr. At the same time, the C^+ flux increases slightly and maximizes as the discharge is carried out in pure N_2 , owing to higher sputter yields of C in nitrogen. As the N_2 content in the sputter gas exceeds 14% the C/Kr/ N_2 plasma is already dominated by N_2^+ and N^+ . Fluxes of both species increase steeply with the N_2 content in the process gas. This is attributed to the low amount of inert gas and target ions due to above discussed reduced ionization rates in

the Kr-containing plasma. Larger C_xN_y ($x, y \leq 2$) species most probably originating from the target^{19,52} increase in fraction with the N_2 content in the sputter gas. For processes employing Kr, their abundance is lower than for processes carried out in Ar-containing atmosphere.

Time-resolved ion mass spectrometry data of the C discharges in Ne and Ne/14% N_2 (1800 W), Ar and Ar/14% N_2 (1800 W), as well as Kr and Kr/14% N_2 (1400 W) are presented in Figs. 7(a)–7(f). Here, time-resolved energy scans were integrated over the whole energy range and presented in dependence of the pulse time. Data were corrected for the TOF within the mass spectrometer as described in Sec. II (Table II). The arrival of the ions at the orifice with regards to the pulse onset depends to a great extent on the target-orifice distance. However, the temporal sequence in which the different ion species appear is based on their energy, size, and origin (target or working gas). Time-resolved ion mass spectrometry data are shown for discharge in pure Ne, Ar, and Kr in Figs. 7(a), 7(c), and 7(e), respectively. Obvious is the rather simultaneous arrival of ionic species related to the C/Ne discharge [Fig. 7(a)], as the bulk of ions in the Ne-containing discharge appears right at the beginning of the pulse, indicating particles with high energies. The main portion of ions related to the Ar-containing discharge [Fig. 7(c)] emerges at $\sim 25 \mu\text{s}$, and in case Kr [Fig. 7(e)] is used, the appearance is further delayed to $\sim 50 \mu\text{s}$ after pulse onset. For discharges in either Ar or Kr, the working gas ions (Ar^+ and Kr^+) are observed well before ($\sim 20 \mu\text{s}$) C^+ ions, and last doubly charged inert gas ions appear. This temporal sequence of working gas and target ions is typically observed for HiPIMS discharges and correlates with the $I(t)$ characteristics of the process.^{19,47,53}

The addition of 14% reactive gas has a strong impact on the temporal evolution on the sputter processes of graphite in Ne and Kr; Figs. 7(b) and 7(f) suggest a delayed arrival (at $\sim 60 \mu\text{s}$ pulse time) for the main portion of ions related to the Ne and Kr processes. In the C/Ne/ N_2 discharge, the first ions arriving at the mass spectrometers orifice are N^+ and

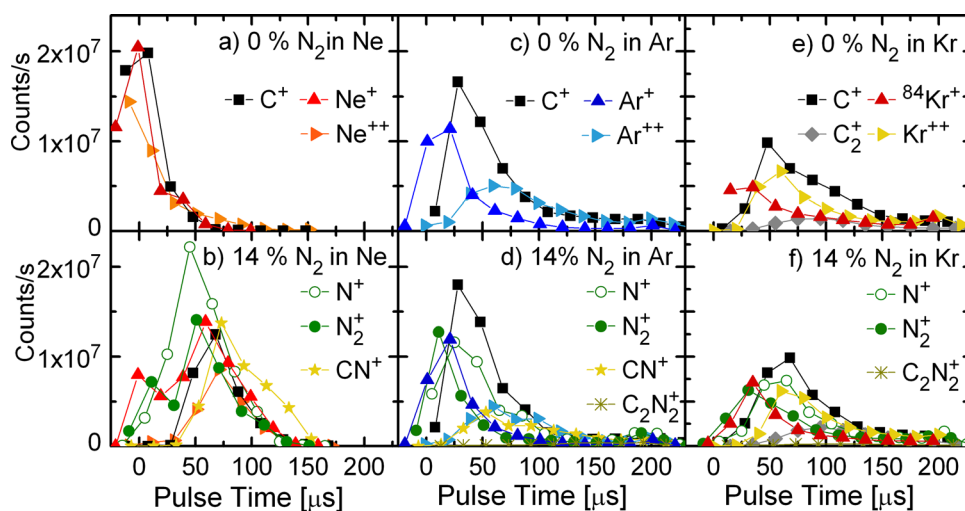


FIG. 7. (Color online) (a)–(f) Total ion count rate vs. pulse time (corresponding to the onset of the pulse) for the graphite discharge in (a) Ne, (b) Ne/14%, (c) Ar, (d) Ar/14% N_2 , (e) Kr, and (f) Kr/14% N_2 . Each data point represents IEDFs recorded during 1 ms and integrated over the entire energy range.

N_2^+ ($\sim 50 \mu s$), closely followed by Ne^+ ($\sim 60 \mu s$) and last are C^+ ($\sim 70 \mu s$), Ne^{++} ($\sim 71 \mu s$), together with CN^+ ($\sim 73 \mu s$). The first species observed in the reactive discharge employing Ar and N_2 are N_2^+ ($\sim 10 \mu s$) and Ar^+ ($\sim 20 \mu s$) followed by N^+ ($\sim 25 \mu s$) together with C^+ ($\sim 30 \mu s$) and, again the last species arriving are CN^+ and Ar^{++} (both $\sim 60 \mu s$). The temporal evolution of the Kr discharge is much more defined in the arrival of working gas ions (Kr^+ isotopes and N_2^+ at $\sim 35 \mu s$) and ions supposedly originating from the target (C^+ , N^+ , and Kr^{++} at $\sim 70 \mu s$) and somewhat later after $\sim 90 \mu s$ C_2^+ . An enhanced representation of the temporal evolution of plasma species of a C/Ar/ N_2 discharge could be extracted from time-resolved ion mass spectroscopy with an increased target-orifice distance of 210 mm.¹⁹ Here, the time windows for working gas ions and ions originating from the target become more distinct with the applied distance. However, in order to get a deeper understanding of the particles origin time-averaged IEDFs should be considered additionally, as the qualitative comparison of the shape might contain valuable information. In the case of Ne, for example, IEDFs of N^+ and C^+ show the similar qualitative features. The corresponding time-resolved data show that a considerable portion of N^+ is arriving together with C^+ . It is thus reasonable to assume that this fraction of N^+ originates from a nitrogen passivated graphite target surface.

C. Impact of inert gases on a-C and CN_x film growth and microstructure

As was demonstrated in Sec. III B, processes employing different inert gases differ to a great extent in particle energy, the amount of C^+ , N^+ , N_2^+ , and inert gas ions as well as in the amount of so-called structure-defining $C_xN_y^+$ species. This implies effects on the film growth and the microstructure of a-C and CN_x thin films, which will be addressed in this section.

In Fig. 8, the deposition rates of a-C (solid square) and CN_x (open triangle) are shown for the three different inert gases as obtained from the ratio of the film thickness (by cross-sectional SEM) and the deposition time. Evident are the low deposition rates for films deposited with HiPIMS in pure Ne and Ne/14% N_2 , compared to those of Ar. Considering the comparatively high sputter yield of C in Ne, the deposition rates should be higher. However, the high ion count rates for the corresponding Ne processes suggest that more material is lost by their back attraction.⁵⁴ Moreover, C^+ , Ne^+ , and N^+ energies in Ne-containing processes [cf. Figs. 3(a), 3(b), and 3(f), gray and black lines, 14% and 0% N_2 in the sputter gas] are 10–12 times higher than those recorded for Ar. This, in combination with the bias voltage of -100 V, which was set for all depositions, increases the energy of ions impinging on the substrate further. Therefore, the physical resputter processes at the substrate may occur to much higher extent in case the graphite target is sputtered in Ne and Ne/14% N_2 atmosphere compared to the corresponding Ar- and Kr-sputter processes. The deposition carried out in pure Kr atmosphere showed a similar rate as the corresponding Ar process. Also, the reactive process in Kr/ N_2

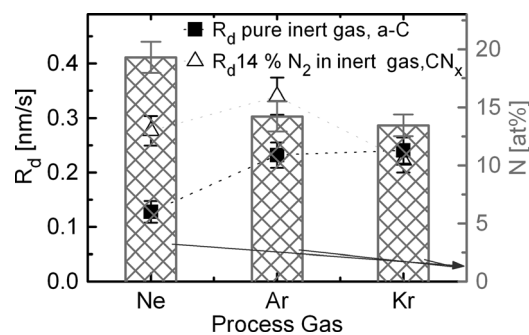


FIG. 8. Deposition rates (R_d) for nonreactive (filled squares) and reactive processes (14% N_2 , open triangles) as obtained from the ratio of film thickness and deposition time as well as the N nitrogen contents ([N]) of CN_x thin films deposited at a substrate temperature of $110^\circ C$ in Ne, Ar, and Kr.

yielded a comparatively low deposition rate. This agrees with similar C sputter yields of C in Kr and Ar.⁵⁵

Moreover, Fig. 8 presents the nitrogen content of the CN_x films for Ne, Ar, and Kr as obtained by ERDA. Obvious is the elevated N content of ~ 19 at. % in the CN_x film deposited in Ne/ N_2 atmosphere. The combination of efficient N_2 dissociation and ionization, and N species of high energy lead to an increased amount of incorporated N. The effect of high particle energies was also observed in ERDA depth profiles (not shown here), as a three times broader substrate/thin film interface was found for the CN_x thin film deposited in Ne compared to that produced in Kr-containing atmosphere. This intermixing of the materials is caused by high particle energies. The CN_x deposition in Kr yields ~ 13 at. % N in the films. This is considered to be a consequence of the reduced N_2 dissociation and ionization in the Kr/14% N_2 plasma. Here, lowered total and relative contents of CN^+ ions as well as N^+ ions were found, indicating decreased amounts of C_xN_y species and dissociated N_2 in the plasma. These species are understood to be key components for the incorporation of nitrogen into the film.

Figure 9 comprises N1s core level photoelectron spectra of CN_x thin films deposited at $430^\circ C$ with 14% N_2 in Kr, Ar, or Ne. A maximum number of four contributions (C1–C4) were fitted into the N1s spectra. The main contributions, C1 (~ 400.5 eV) and C2 (398.1–398.6 eV), are assigned to nitrogen substitutionally bonded in a 3-fold coordinated C-network (e.g., N bonded into a sp^2 -coordinated carbon plane) and a sp^2 -hybridized nitrogen bonded with two bonds to the C-network (pyridine-like), respectively.^{56,57} The bonding configuration associated with C2 arises next to defects or at the periphery of the graphene sheets, breaking their continuity. As indicated in Fig. 9, the C1/C2 increases with decreasing amount of incorporated N in the film (values for [N] at $430^\circ C$ are given in Fig. 9) and increasing inert gas mass. C1/C2 is greater than one for Ar- and Kr-containing processes. The structural arrangement of thin films is correlated to the C1/C2 ratio.⁵⁶ Increased C1/C2 ratios indicate a pronounced fullerene-like structural evolution, since C1 (~ 400.5 eV) is attributed to N substitutionally bonded in extended carbon sheets, while C2 (~ 398.2 eV) is attributed to N bonded along edges and defects.^{56,57} For CN_x thin films deposited in either

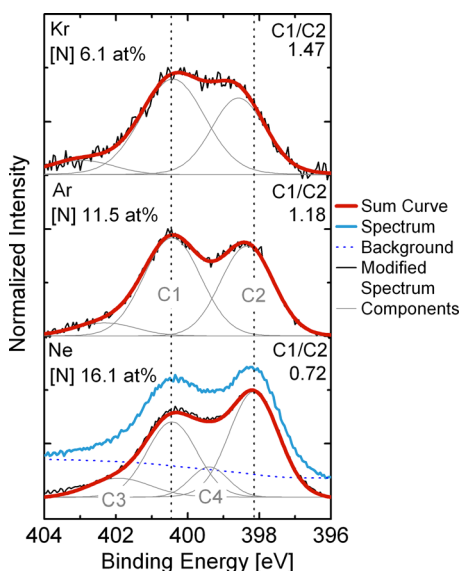


Fig. 9. (Color online) XPS N1s spectra of CN_x thin films deposited using reactive HiPIMS and a substrate temperature of 430 °C in Ne, Ar, and Kr containing 14% N_2 . The peak deconvolution, the N content in the CN_x thin films, and the C1/C2 ratios of the corresponding films are indicated.

Kr- or Ar-containing atmosphere, the C1/C2 ratios are higher than 1, indicating that both CN_x films exhibit a FL-structure. This is conceivable as both processes showed low ion energies (cf. Sec. III B) preserving structure-defining C_xN_y -species ($x, y \leq 2$) in the plasma, which in turn promote the chemical desorption processes at the substrate. Especially, the Kr process was governed by low energy ions, which is mirrored in the comparably high C1/C2 ratio of 1.47. In contrast to the high C1/C2 ratio observed for CN_x obtained in Kr-containing atmosphere, C1 and C2 appear broadened, additionally, C2 shifts toward higher binding energies. Both usually imply amorphous structures and were observed in thin films deposited at temperatures below 300 °C.⁵⁶

The deposition of CN_x thin films in Ne-containing atmosphere yields C1/C2 < 1, indicating an amorphous structure with frequently disrupted graphene sheets. This correlates with IEDFs recorded for the C/Ne/14% N_2 plasma consisting mainly of ions exhibiting high energies, which in turn are

likely to destroy a structural evolution of the thin films. The assignment of C3, a minor contribution arising between 403 eV and 402 eV, is not consistent in literature. C3 is reported to arise either from N-O (Ref. 11) bonds or due to a similar substitutional bonding configuration as described for C1, except that the nitrogen donates an electron to the structure; thus, the C3 peak appears at higher binding energies and scales with C1.^{11,57} C4 (~399 eV) is assigned to sp-hybridized nitrogen in a nitrile⁵⁷ structure. Only for CN_x thin films deposited in Ne-containing atmosphere C4 could be fitted. This correlates with high amounts of incorporated N into the film.

Figures 10(a)–10(c) show selected HRTEM images with corresponding SAED patterns from the samples analyzed by XPS and presented in Fig. 9. The comparison of the relative intensities of diffuse SEAD rings provides information about the degree and extension of the graphitic short range order of CN_x films.⁴¹ The peak intensity ratio $I_{3.5 \text{ \AA}}/I_{2 \text{ \AA}}$ (R) provides a parameter for the quantitative comparison of the microstructure. The evaluation of SAED pattern revealed R to be highest (>1) for CN_x thin films deposited in Ar ($R \sim 2$) and Kr ($R \sim 1$) and $R < 1$ for CN_x when Ne ($R \sim 0$) was employed as sputter gas. The results extracted from the SAED pattern are also reflected in the corresponding HRTEM images, as these reveal a FL structure for thin films sputtered in Ar- [Fig. 10(b)] or Kr-containing atmosphere [Fig. 10(c)] and an amorphous thin film for the CN_x thin film produced in Ne/ N_2 [Fig. 10(a)].

The relative intensity of the $\sim 3.5 \text{ \AA}$ peak correlates with the C1/C2 ratio of the XPS N1s regions as observed for DC sputtered CN_x films.⁵⁶ However, the correlation is not satisfactory, if merely the XPS C1/C2 ratio is taken into account, since CN_x films deposited in Ar/14% N_2 seem to possess a more pronounced fullerene-like structure by HRTEM and SAED ($R \sim 2$) than that deposited in Kr/14% N_2 ($R \sim 1$), although the C1/C2 ratio for the thin film deposited in Kr-containing atmosphere is higher. Thus, as pointed out above, the peak broadening of C1 and C2 as well as the shift of C2 toward higher binding energies for the 14% N_2 /Kr process should also be taken into account, as both are signs of a less ordered structure.⁵⁷

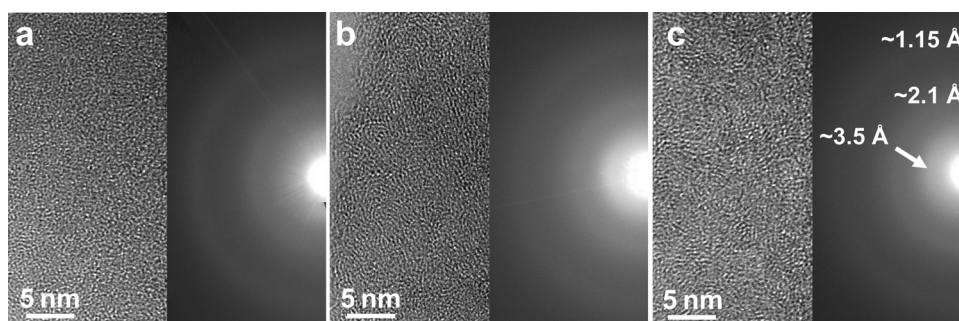


Fig. 10. (a)–(c) Cross-sectional HRTEM images with corresponding SAED patterns from CN_x thin films deposited by HiPIMS at $T_s = 430 \text{ °C}$ in 14% N_2 and different inert gases: (a) 14% N_2 /Ne, (b) 14% N_2 /Ar, and (c) 14% N_2 /Kr. SAED labels in (c) mark the position of ~ 1.15 and $\sim 2.1 \text{ \AA}$ diffuse rings. The arrow indicates the brightest segment of the $\sim 3.5 \text{ \AA}$ ring, which implies a slightly textured graphitic ordering (with preferred orientation of basal planes perpendicular to the substrate). The growth direction in the HRTEM images shows upwards. The films deposited in Ar and Kr have the most pronounced fullerene-like structure.

IV. CONCLUSIONS

Reactive HiPIMS of C in the inert gases Ne, Ar, and Kr yield distinctly different discharges. The $I(t)$ discharge characteristics of the inert gases show increasing target currents with decreasing atomic number, mainly caused by different I_P as well as ionization pathways and cross sections. The most abundant precursors in reactive processes are C^+ , N^+ , N_2^+ , single and double charged inert gas ions, and to a lower extent CN^+ . The IEDFs of the corresponding discharges when no N_2 is involved exhibit increasing energies with decreasing atomic number of the inert gas. When the N_2 content of the C/Ne-HiPIMS discharge exceeds 14%, the energy of C^+ , Ne^+ , and N^+ decreases significantly, since Penning ionization of N_2 disappears gradually for increasing N_2 concentrations in the working gas. When N_2 is added to the Ar and Kr processes, the energy of the IEDFs increases with increasing N_2 content in the sputter gas. However, Ne- and Kr-containing discharges are more affected by the reactive gas than it is the case for Ar. This can be attributed to much higher differences in I_P and the total ionization cross sections for Ne and Kr with regards to N_2 and N than for Ar. The total amount of ions increases in the sequence Kr, Ar, and Ne because of the increasing ionization potential that causes a higher electron temperature of the corresponding plasma and thus, an improved ionization. Additionally, the energy of metastable states increases in the same sequence, which allows only Ne to Penning ionize and excite N_2 , implicating its highly efficient dissociation. This is mirrored in the amplified abundance of C_xN_y species ($x, y \leq 2$) of the Ne-containing plasma above 33% N_2 in the gas. The relative, but not the total C^+ ion flux is highest in case the graphite target is sputtered in pure Ar, followed by Ne and Kr. Independent from the inert gas, the relative C^+ flux decreases in reactive sputter mode and shows a minimum between 33% and 50% of N_2 in the plasma, in consequence of increasing N^+ and N_2^+ fluxes. The relative fluxes of N^+ increase with decreasing atomic number of the inert gas, while the relative flux of N_2^+ shows the opposite trend owing to the increased ability of Ne to dissociate N_2 . The deposition rates are highest as C is sputtered in Kr- or Ar-containing atmosphere, while processes in Ne yield the lowest deposition rates, which we attribute to back attraction and to physical resputtering due to the high amount and energy of the particles arriving at the substrate. Reactive processes with 14% N_2 in either Ne or Ar yield increased deposition rates, whereas similar deposition rates were found for reactive and nonreactive processes involving Kr. The amount of incorporated N in the CN_x thin films is highest for Ne-containing processes, which is attributed to a combination of efficient N_2 dissociation and ionization, and N species of high energy that lead to an increased probability for incorporated N in a pyridine- and nitrile-like manner. We also find a relative increase of substitutional bonded nitrogen in a 3-fold coordinated C network with atomic number of the inert gas, accounting for a pronounced FL-structure of the thin film. This is also mirrored in TEM and SAED results; amorphous CN_x thin films were obtained for the process with Ne/14% N_2 , whereas gas

mixtures involving Ar/14% N_2 or Kr/14% N_2 yielded FL- CN_x thin films. Ion mass spectrometry, XPS, and TEM results emphasize the crucial role of low particle energies generated in the plasma and N-containing precursor species (C_xN_y) for the structural evolution of CN_x thin films.

ACKNOWLEDGMENTS

An ERC Advanced Grant and the VINN Excellence Center *Functional Nanoscale Materials (FunMat)* are acknowledged. With regards to ERDA measurements, the authors are thankful for the access to the Tandem Laboratory, Uppsala University. Zsolt Czigány acknowledges the Bolyai Scholarship of the Hungarian Academy of Sciences.

- ¹Y. Lifshitz, *Diam. Relat. Mater.* **5**, 388 (1996).
- ²J. Robertson, *Phys. Rev. Lett.* **68**, 220 (1992).
- ³J. Robertson, *Jpn. J. Appl. Phys.* **50**, 8 (2011).
- ⁴N. Hellgren, M. P. Johansson, B. Hjorvarsson, E. Broitman, M. Ostblom, B. Liedberg, L. Hultman, and J. E. Sundgren, *J. Vac. Sci. Technol. A* **18**, 2349 (2000).
- ⁵J. Neidhardt and L. Hultman, *J. Vac. Sci. Technol. A* **25**, 633 (2007).
- ⁶J. C. Angus and C. C. Hayman, *Science* **241**, 913 (1988).
- ⁷J. Robertson, *Adv. Phys.* **35**, 317 (1986).
- ⁸J. Robertson, *Mater. Sci. Eng. R* **37**, 129 (2002).
- ⁹A. Grill, *Diam. Relat. Mater.* **12**, 166 (2003).
- ¹⁰J. Neidhardt, L. Hultman, E. Broitman, T. W. Scharf, and I. L. Singer, *Diam. Relat. Mater.* **13**, 1882 (2004).
- ¹¹L. Hultman, J. Neidhardt, N. Hellgren, H. Sjoström, and J. E. Sundgren, *MRS Bull.* **28**, 194 (2003).
- ¹²M. C. Polo, J. L. Andujar, A. Hart, J. Robertson, and W. I. Milne, *Diam. Relat. Mater.* **9**, 663 (2000).
- ¹³J. Robertson, *Prog. Solid State Chem.* **21**, 199 (1991).
- ¹⁴Y. Lifshitz, S. R. Kasi, J. W. Rabalais, and W. Eckstein, *Phys. Rev. B* **41**, 10468 (1990).
- ¹⁵P. J. Fallon, V. S. Veerasamy, C. A. Davis, J. Robertson, G. A. J. Amarantunga, W. I. Milne, and J. Koskinen, *Phys. Rev. B* **48**, 4777 (1993).
- ¹⁶J. Robertson, *Diam. Relat. Mater.* **2**, 984 (1993).
- ¹⁷J. T. Gudmundsson, N. Brenning, D. Lundin, and U. Helmersson, *J. Vac. Sci. Technol. A* **30**, 030801 (2012).
- ¹⁸U. Helmersson, M. Lättemann, J. Bohlmark, A. P. Ehiasarian, and J. T. Gudmundsson, *Thin Solid Films* **513**, 124 (2006).
- ¹⁹S. Schmidt, Z. Czigany, G. Greczynski, J. Jensen, and L. Hultman, *J. Appl. Phys.* **112**, 013305-11 (2012).
- ²⁰B. M. DeKoven, P. R. Ward, R. E. Weiss, D. J. Christie, R. A. Scholl, W. D. Sproul, F. Tomasel, and A. Anders, in *46th Annual Technical Conference Proceedings*, San Francisco, CA (Society of Vacuum Coaters, 2003), pp. 158–165.
- ²¹K. Sarakinos, A. Braun, C. Zilkens, S. Mraz, J. M. Schneider, H. Zoubos, and P. Patsalas, *Surf. Coat. Technol.* **206**, 2706 (2012).
- ²²I. Petrov, L. Ivanov, V. Orlov, J. Kourtev, and J. Jelev, *Thin Solid Films* **185**, 247 (1990).
- ²³A. Aijaz, K. Sarakinos, D. Lundin, N. Brenning, and U. Helmersson, *Diam. Relat. Mater.* **23**, 1 (2012).
- ²⁴K. J. Taylor, S. M. Yun, and G. R. Tynan, *J. Vac. Sci. Technol. A* **22**, 2131 (2004).
- ²⁵K. Ohya, *Nucl. Instrum. Meth. Phys. Res. B* **206**, 52 (2003).
- ²⁶J. C. Avelar-Batista, A. D. Wilson, A. Davison, A. Leyland, A. Matthews, and K. S. Fancey, *Thin Solid Films* **398–399**, 507 (2001).
- ²⁷F. M. Penning and C. C. J. Addink, *Physica* **1**, 1007 (1934).
- ²⁸K. S. Fancey, *Vacuum* **46**, 695 (1995).
- ²⁹J. Nagai, J. C. Thomaz, J. Amorim, and G. Baravian, *Eur. Phys. J.* **26**, 53 (2004).
- ³⁰G. K. Gueorguiev, J. Neidhardt, S. Stafstrom, and L. Hultman, *Chem. Phys. Lett.* **410**, 228 (2005).
- ³¹M. Schlueter, C. Hopf, and W. Jacob, *New J. Phys.* **10**, 053037 (2008).
- ³²J. Bohlmark, M. Lättemann, J. T. Gudmundsson, A. P. Ehiasarian, Y. A. Gonzalvo, N. Brenning, and U. Helmersson, *Thin Solid Films* **515**, 1522 (2006).

- ³³N. Hellgren, M. P. Johansson, E. Broitman, L. Hultman, and J.-E. Sundgren, *Phys. Rev. B* **59**, 5162 (1999).
- ³⁴N. Hellgren, M. P. Johansson, E. Broitman, P. Sandstrom, L. Hultman, and J. E. Sundgren, *Thin Solid Films* **382**, 146 (2001).
- ³⁵H. J. Whitlow, G. Possnert, and C. S. Petersson, *Nucl. Instrum. Meth. Phys. Res. B* **27**, 448 (1987).
- ³⁶J. Jensen, D. Martin, A. Surpi, and T. Kubart, *Nucl. Instrum. Meth. Phys. Res. B* **268**, 1893 (2010).
- ³⁷Z. Czigany, J. Neidhardt, I. F. Brunell, and L. Hultman, *Ultramicroscopy* **94**, 163 (2003).
- ³⁸E. Broitman, N. Hellgren, J. Neidhardt, I. Brunell, and L. Hultman, *J. Electron. Mater.* **31**, L11 (2002).
- ³⁹J. P. McCaffrey, *Microsc. Res. Techn.* **24**, 180 (1993).
- ⁴⁰J. L. Labar, *Microsc. Microanal.* **15**, 20 (2009).
- ⁴¹Z. Czigany and L. Hultman, *Ultramicroscopy* **110**, 815 (2010).
- ⁴²D. Rapp and P. Englander-Golden, *J. Chem. Phys.* **43**, 1464 (1965).
- ⁴³D. M. Mattox, *Handbook of Physical Vapor Deposition (PVD) Processing* (Noyes, Park Ridge, NJ, 1998).
- ⁴⁴A. Anders, *Surf. Coat. Technol.* **205**, S1 (2011).
- ⁴⁵J. T. Gudmundsson, J. Alami, and U. Helmersson, *Surf. Coat. Technol.* **161**, 249 (2002).
- ⁴⁶A. Hecimovic and A. P. Ehiasarian, *IEEE Trans. Plasma Sci.* **39**, 1154 (2011).
- ⁴⁷M. Hala, N. Viau, O. Zabeida, J. E. Klemberg-Sapieha, and L. Martinu, *J. Appl. Phys.* **107**, 9 (2010).
- ⁴⁸G. Lempérière and J. M. Poitevin, *Vacuum* **37**, 825 (1987).
- ⁴⁹A. Hecimovic, K. Burcalova, and A. P. Ehiasarian, *J. Phys. D* **41**, 10 (2008).
- ⁵⁰N. Itagaki, S. Iwata, K. Muta, A. Yonesu, S. Kawakami, N. Ishii, and Y. Kawai, *Thin Solid Films* **435**, 259 (2003).
- ⁵¹S. Yoon and W. L. Glab, *J. Phys. B* **27**, 4133 (1994).
- ⁵²J. Neidhardt, L. Hultman, B. Abendroth, R. Gago, and W. Moller, *J. Appl. Phys.* **94**, 7059 (2003).
- ⁵³G. Greczynski and L. Hultman, *Vacuum* **84**, 1159 (2010).
- ⁵⁴N. Brenning, C. Huo, D. Lundin, M. A. Raadu, C. Vitelaru, G. D. Stancu, T. Minea, and U. Helmersson, *Plasma Sources Sci. Technol.* **21**, 025005 (2012).
- ⁵⁵E. Oyarzabal, R. P. Doerner, M. Shimada, and G. R. Tynan, *J. Appl. Phys.* **104**, 043305 (2008).
- ⁵⁶J. Neidhardt, L. Hultman, and Z. Czigany, *Carbon* **42**, 2729 (2004).
- ⁵⁷N. Hellgren, J. H. Guo, Y. Luo, C. Sathe, A. Agui, S. Kashtanov, J. Nordgren, H. Agren, and J. E. Sundgren, *Thin Solid Films* **471**, 19 (2005).
- ⁵⁸R. Rejoub, B. G. Lindsay, and R. F. Stebbings, *Phys. Rev. A* **65**, 042713 (2002).
- ⁵⁹Y.-K. Kim and J.-P. Desclaux, *Phys. Rev. A* **66**, 012708 (2002).
- ⁶⁰J. F. Ziegler, <http://www.srim.org/>, v. srim 2008 (November 2012).